source rocks of this material (0.25 and 0.12, respectively). The recycling rate inferred from the $F(t)$ constraint is too small to explain the discrepancy between the observed and inferred Sm/Nd ratios in each reservoir. Therefore, Nd isotopic evolution of the upper mantle is controlled not only by recycling of continental crust but also by exchange of material with a different reservoir (*21*) with a low $^{147}Sm/^{144}Nd$ ratio, which could be material segregated from subducted lithospheric plates (*22*) or a deep layer left behind by early terrestrial differentiation (*23*).

These constraints from the ^{40}Ar budget of the observable reservoirs depend on the very incompatible behavior of K and Ar and therefore are robust. Only if Ar were substantially more compatible than K would the conclusions be clearly inadequate. The solubility of Ar in olivine melt actually may decrease dramatically beyond 4 to 5 GPa (*24*). Partial melting possibly extended at 150 to 200 km in the past because the mantle was hotter, especially under the MORs. So far, however, the compatible behavior of ^{40}Ar during melting remains to be demonstrated and the constraints on the rate of continental growth and mantle degassing given by the ^{40}Ar and K budget remain.

References and Notes

1. D. K. Rea and L. J. Ruff, *Earth Planet. Sci. Lett*. **140**, 1 (1996); T. Plank and C. H. Langmuir, *Chem. Geol*. **145**, 325 (1998) and references therein.
2. R. von Huene and D. W. Scholl, *Rev. Geophys*. **29**, 279 (1991).
3. A. Reymer and G. Schubert, *Tectonics* **3**, 63 (1984).
4. G. Schubert and D. Sandwell, *Earth Planet. Sci. Lett*. **92**, 234 (1989).
5. D. DePaolo, *Geophys. Res. Lett*. **10**, 705 (1983).
6. F. Albarède, *Tectonophysics* **161**, 299 (1989).
7. C. J. Allègre, A. W. Hofmann, R. K. O'Nions, *Geophys. Res. Lett*. **23**, 3555 (1996).
8. D. W. Schwartzman, *Geochim. Cosmochim. Acta* **37**, 2479 (1973).
9. H. Craig, W. B. Clarke, W. A. Beg, *Earth Planet. Sci. Lett*. **26**, 125 (1975); E. R. Oxburgh, R. K. O'Nions, R. I. Hill, *Nature* **324**, 632 (1986); P. Jean Baptiste *et al.*, *Earth Planet. Sci. Lett*. **106**, 17 (1991); A. Jambon, *Rev. Mineral*. **30**, 379 (1994).
10. A. W. Hofmann, *Earth Planet. Sci. Lett*. **90**, 297 (1988); H. Hiyagon and M. Ozima, *Geochim. Cosmochim. Acta* **50**, 2945 (1986); R. A. Brooker, J. A. Wartho, M. R. Carroll, S. P. Kelley, *Chem. Geol*. **147**, 185 (1998).
11. H.-C. Nataf and Y. Ricard, *Phys. Earth Planet. Int*. **95**, 101 (1996); W. D. Mooney, G. Laske, T. G. Master, *J. Geophys. Res*. **103**, 727 (1998).
12. K. Turekian, *Geochim. Cosmochim. Acta* **17**, 37 (1959).
13. R. L. Rudnick and D. M. Fountain, *Rev. Geophys*. **33**, 267 (1995).
14. K. H. Weaver and J. Tarney, *Nature* **310**, 575 (1984); D. M. Shaw, J. J. Cramer, M. D. Higgins, M. G. Truscott, in *The Nature of the Lower Continental Crust*, J. B. Dawson, Ed. (Geological Society of London, London, 1986), pp. 257–282.
15. K. H. Wedepohl, *Mineral. Mag*. **58**, 959 (1994).
16. S. R. Taylor and S. M. McLennan, *The Continental Crust: Its Composition and Evolution* (Blackwell, Cambridge, 1985).
17. J. G. Sclater, C. Jaupart, D. Galson, *Rev. Geophys*. **18**, 269 (1980).
18. The radioactive production rate $\lambda R\ ^{40}K_{mantle}$ assuming a K content of the mantle of 240 parts per million as in [W. F. McDonough and S. Sun, *Chem. Geol*. **120**, 223 (1995)].
19. C. J. Allègre, T. Staudacher, P. Sarda, *Earth Planet. Sci. Lett*. **81**, 127 (1986/1987).
20. P. Burnard, D. Graham, G. Turner, *Science* **276**, 568 (1997); P. Sarda, M. Moreira, T. Staudacher, *Science* **283**, 666 (1999).
21. It has been argued that comparison of the Th/U ratio of MOR basalts with that inferred from their values of $^{208}Pb/^{204}Pb$ and $^{230}Th/^{232}Th$ [S. J. G. Galer and R. K. O'Nions, *Nature* **316**, 778 (1985)] indicates chemical buffering of the upper mantle by the lower mantle, but this model depended entirely on the assumption of complete removal of Pb, U, and Th at the subduction zone by orogenic volcanism. Similarly, the possibility that the upper mantle and the deep mantle were exchanging material through the 660-km discontinuity was also considered [P. J. Patchett and C. Chauvel, *Geophys. Res. Lett*. **11**, 151 (1984)] as an alternative to DePaolo's interpretation of Nd and Hf isotopic secular evolution, but this lower mantle was then considered to be of primitive composition, which modern mantle tomography makes untenable [R. D. van der Hilst, S. Widiyantoro, E. R. Engdahl, *Nature* **386**, 578 (1997)].
22. U. R. Christensen and A. W. Hofmann, *J. Geophys. Res*. **99**, 19867 (1994); T. Elliott, A. Zindler, B. Bourdon, *Earth Planet. Sci. Lett*. **169**, 129 (1999); N. Coltice and Y. Ricard, *Earth Planet. Sci. Lett*. **174**, 125 (1999).
23. L. H. Kellogg, B. H. Hager, R. D. van der Hilst, *Science* **283**, 1881 (1999).
24. E. Chamorro-Pérez, P. Gillet, A. Jambon, J. Badro, P. McMillan, *Nature* **393**, 352 (1998).

25. We thank A. Jambon for his comments on this work.

6 January 2000; accepted 20 March 2000

Satellite Measurements of Sea Surface Temperature Through Clouds

Frank J. Wentz,[1] Chelle Gentemann,[1] Deborah Smith,[1] Dudley Chelton[2]

Measurements of sea surface temperature (SST) can be made by satellite microwave radiometry in all weather conditions except rain. Microwaves penetrate clouds with little attenuation, giving an uninterrupted view of the ocean surface. This is a distinct advantage over infrared measurements of SST, which are obstructed by clouds. Comparisons with ocean buoys show a root mean square difference of about 0.6°C, which is partly due to the satellite-buoy spatial-temporal sampling mismatch and the difference between the ocean skin temperature and bulk temperature. Microwave SST retrievals provide insights in a number of areas, including tropical instability waves, marine boundary layer dynamics, and the prediction of hurricane intensity.

The surface temperature of the world's oceans plays a fundamental role in the exchange of energy, momentum, and moisture between the ocean and the atmosphere. It is a central determinant of air-sea interactions and climate variability. The recurring El Niño–La Niña cycle, which has a profound effect on the world's weather and climate, is a dramatic manifestation of the coupling of SST to atmospheric circulation (*1*, *2*). The surface temperature field also influences the development and evolution of tropical storms and hurricanes (*3*, *4*) and is correlated with nutrient concentration and primary productivity (*5*).

Satellite measurements of SST began in the 1970s, using infrared radiometers flying aboard the National Oceanic and Atmospheric Administration's geostationary and polar orbiting platforms (*6*). Satellite infrared SST measurements have resulted in major advancements in oceanography, meteorology, and climatology (*2*, *7–10*). However, the infrared SST retrievals have two significant limitations: (i) Retrievals cannot be done when clouds (which cover roughly half the Earth) are present. (ii) Atmospheric aerosols from volcanoes and large fires can cause a spurious cooling in the SST retrieval (*11*, *12*). The aerosol problem has been particularly troublesome when trying to construct multiyear time series to infer climate change (*11*). Furthermore, the cloud detection algorithms are not totally reliable, with some clouds going undetected.

It has long been recognized that microwave radiometry offers a solution to the cloud and aerosol problem. At frequencies below about 12 GHz, the surface radiance is proportional to SST and microwaves penetrate clouds with little attenuation, giving a clear view of the sea surface under all weather conditions except rain. Furthermore, at these frequencies, atmospheric aerosols have no effect, making it possible to produce a very reliable SST time series for climate studies. The first satellite microwave radiometers operating at these low frequencies were flown on SeaSat and Nimbus-7, launched in 1978. These early missions demonstrated the

[1]Remote Sensing Systems, 438 First Street, Suite 200, Santa Rosa, CA 95401, USA. [2]College of Oceanic and Atmospheric Sciences, Oregon State University, Corvallis, OR 97331, USA.

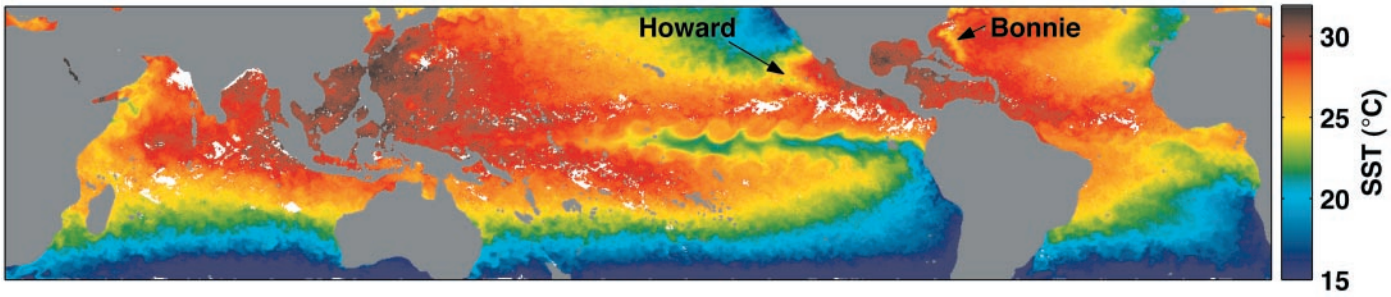

Fig. 1. The SST field for 25 to 27 August 1998, as seen by TMI from 40°S to 40°N. Areas of persistent rain are indicated by white. The equatorial cold tongue in the eastern Pacific is bordered on the north and south by TIWs propagating from South America westward to about 160°E. Also discernible are the cold wakes of Hurricane Bonnie in the west Atlantic and of Cyclone Howard in the east Pacific as well as strong monsoonal upwelling off the coast of Arabia and Somalia.

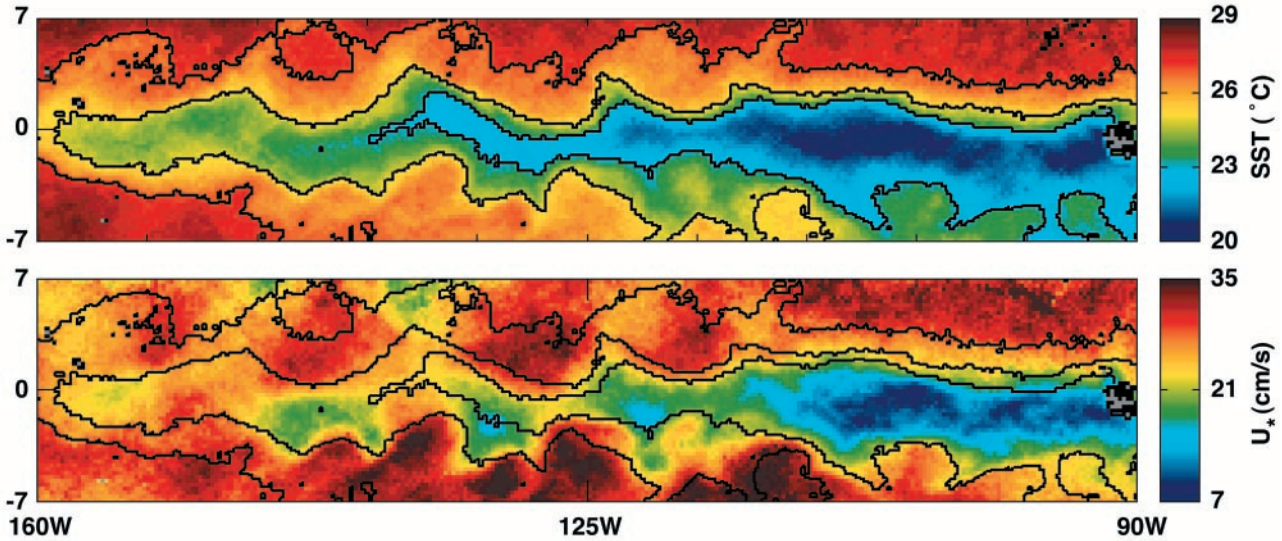

Fig. 2. SST and surface wind in the vicinity of the eastern Pacific equatorial cold tongue during the first week in October 1998. The surface wind is given in terms of the friction velocity U_*. The black contour lines show the isotherms for 23°, 25°, and 27°C derived from the SST image. These contour lines are superimposed on the U_* image to highlight its correlation with SST. Both SST and wind clearly delineate the TIWs to the north and south of the cold tongue. Over warm water, turbulent mixing increases the exchange of momentum from winds aloft to the surface. As a result, higher surface winds are associated with warmer water.

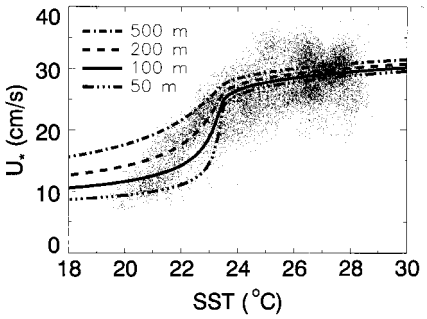

Fig. 3. A scatter plot of the weekly averaged values of U_* versus SST shown in Fig. 2. The spatial resolution of each value is 50 km. The four curves show the U*-versus-SST relation given by a boundary layer model (*26*) having a thickness of 50 to 500 m. The air temperature and wind speed at the top of the boundary layer are assumed to be 24°C and 9 m/s, respectively.

feasibility of measuring SST with microwaves (*13*, *14*) and led to some notable scientific results (*15*). However, the usefulness of these early radiometers was significantly limited by a poor calibration system. Subsequent microwave radiometers launched in the 1980s and 1990s, such as the Special Sensor Microwave Imager (SSM/I), used improved calibration systems but lacked the low-frequency channels needed to retrieve SST. In November 1997, the Tropical Rainfall Measuring Mission (TRMM) spacecraft was launched (*16*). The TRMM microwave imager (TMI) has a full suite of channels ranging from 10.7 to 85 GHz and represents the first satellite sensor that is capable of accurately measuring SST through clouds.

Retrieval of SST from the microwave radiances requires that the influence of atmospheric attenuation and sea surface roughness be removed from the observations. A physically based retrieval algorithm is used to remove these effects (*17*). When rain is not present, the attenuation is very small at 10.7 GHz, with 97% of the sea surface radiation reaching the top of the atmosphere. Using the higher frequency channels (19 to 37 GHz), the algorithm precisely estimates the 3% attenuation due to oxygen, water vapor, and clouds. The polarization ratio (horizontal versus vertical) of the measurements is used to estimate sea surface roughness. The spatial resolution of the SST retrieval is limited by the ratio of the radiation wavelength to the antenna diameter and by the satellite altitude. For TMI, the spatial resolution is about 50 km. This relatively coarse resolution is the major limitation of microwave SST retrievals as compared to infrared retrievals, which have higher resolutions of 1 to 10 km.

Raindrops, which have a much larger diameter than cloud droplets, can significantly attenuate and scatter microwave radiation. As a result, SST retrievals are not reliable when rain is present. The 37-GHz channels are very sensitive to rain and are used to determine when rain is in the radiometer's field of view. When rain is detected, the SST retrieval is discarded.

The SST retrievals were validated by direct comparison with ocean buoys (*18*, *19*) for the period from December 1997 to June 1999. The root mean square (rms) difference

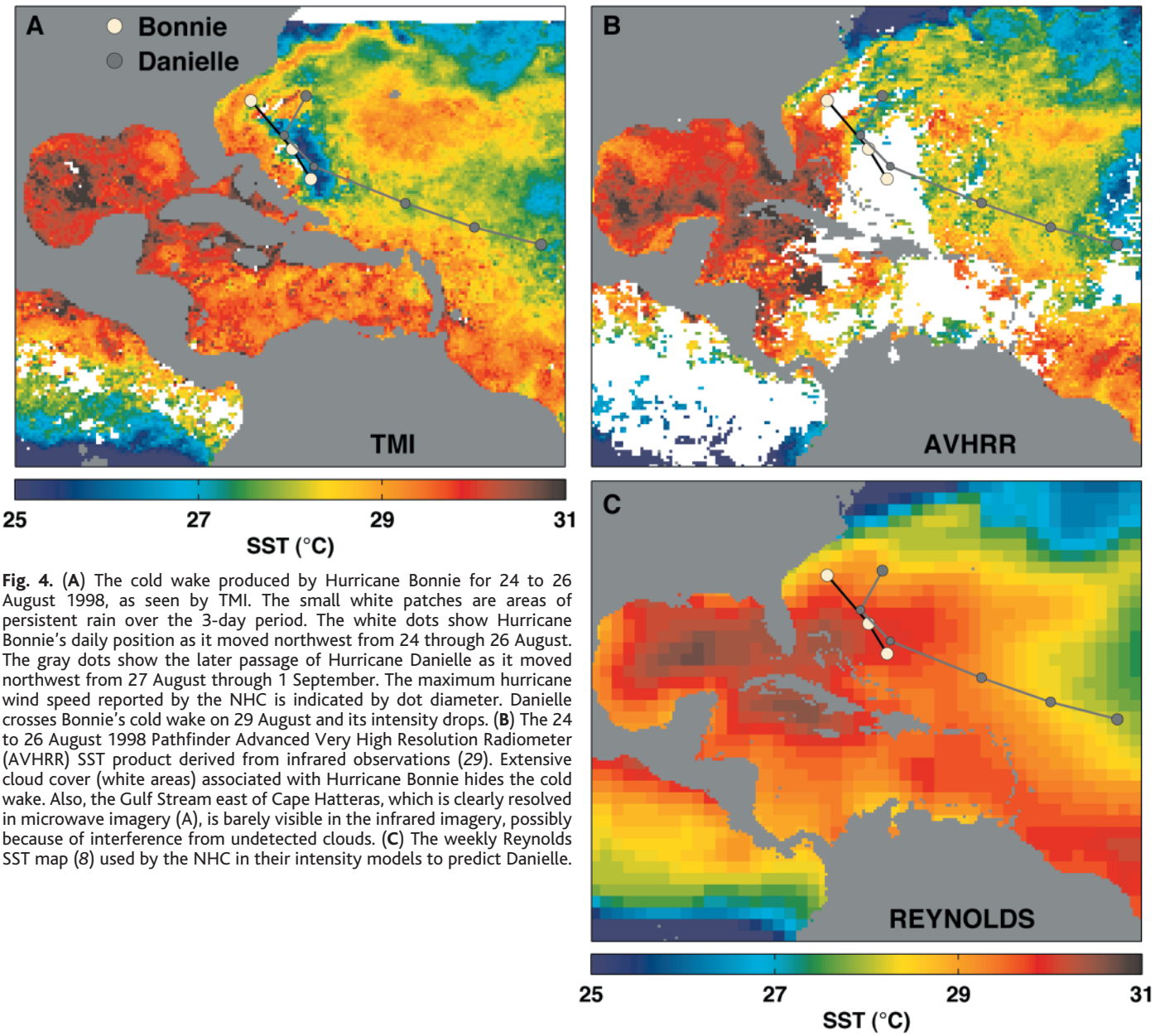

Fig. 4. (**A**) The cold wake produced by Hurricane Bonnie for 24 to 26 August 1998, as seen by TMI. The small white patches are areas of persistent rain over the 3-day period. The white dots show Hurricane Bonnie's daily position as it moved northwest from 24 through 26 August. The gray dots show the later passage of Hurricane Danielle as it moved northwest from 27 August through 1 September. The maximum hurricane wind speed reported by the NHC is indicated by dot diameter. Danielle crosses Bonnie's cold wake on 29 August and its intensity drops. (**B**) The 24 to 26 August 1998 Pathfinder Advanced Very High Resolution Radiometer (AVHRR) SST product derived from infrared observations (*29*). Extensive cloud cover (white areas) associated with Hurricane Bonnie hides the cold wake. Also, the Gulf Stream east of Cape Hatteras, which is clearly resolved in microwave imagery (A), is barely visible in the infrared imagery, possibly because of interference from undetected clouds. (**C**) The weekly Reynolds SST map (*8*) used by the NHC in their intensity models to predict Danielle.

between the daily averaged buoy and satellite SSTs ranged from 0.5° to 0.7°C (Table 1). The satellite-buoy difference is due to a number of effects, including errors in the satellite retrievals, the spatial-temporal mismatch between the buoy point observation and the satellite's 50-km footprint, and the difference between the ocean skin temperature and the bulk temperature measured by the buoys at 1 to 1.5 m depth (*20*). The instrument noise in the satellite retrievals, which can be reduced through more spatial-temporal averaging, contributes about 0.3°C (in a root-sum-squared sense) to the overall observed difference.

An example of the SST field derived from TMI is shown in Fig. 1. The field of view is limited to 40°S and 40°N, because a low inclination orbit was chosen for continuous monitoring of the tropics. Except for a few small areas of persistent rain, TMI provides complete coverage in three days. The most striking feature in the figure is the tropical instability waves (TIWs) in the equatorial eastern Pacific both north and south of the equatorial cold tongue (*7*). TIWs are westward-propagating waves that are most likely generated by instabilities in the equatorial ocean current/countercurrent system (*21*). For these ocean waves to be visible in SST imagery, there must be an appreciable meridional SST gradient, which was unusually strong due to the 1998 La Niña. TMI is providing an unprecedented view of the evolution of TIWs in both the Pacific and Atlantic Oceans (*22*). Also apparent in the figure are cold wakes from two active tropical cyclones. The strong winds drive oceanic turbulent mixing and upwelling, resulting in a cold track just to the right of the cyclone path. Intense upwelling, driven by a low-level atmospheric monsoonal jet, is also visible along the coast of Arabia and Somalia.

Table 1. Comparisons of TMI SST retrievals with collocated buoys. Results are shown for three buoy arrays: Tropical Atmospheric Ocean (TAO) (*18*), Pilot Research Moored Array (PIRATA), and the National Buoy Data Center (NDBC) (*19*).

Buoy array	Number of observations	Mean difference	SD
TAO	1479	−0.27	0.51
NDBC	3307	0.01	0.70
PIRATA	1393	0.02	0.49

Microwave observations are an ideal way to observe the interaction between SST and

wind because both variables can be simultaneously retrieved. Previous analyses of the TIWs and the cold tongue have shown a close coupling between SST and wind and have suggested that the coupling is due to marine boundary layer (MBL) dynamics rather than to pressure gradients (*23*–*25*). Over warm water, the MBL is unstable, air turbulence enhances the exchange of momentum from winds aloft to the surface, and higher surface winds result. For cold water, the boundary is stable, the vertical exchange of momentum is less, and the surface winds are lower. TMI SST and wind fields (Fig. 2) reveal how highly correlated SST-wind couplings are on a much finer temporal-spatial scale (measured weekly at a resolution of 50 km) than previously reported. The linear correlation between the weekly SST and the surface wind at a resolution of 50 km is 0.78, and the observed relation between SST and wind is consistent with a relatively simple boundary layer model (Fig. 3) (*26*).

Cold wakes from storms and hurricanes have been studied in the past by means of infrared SST observations (*10*, *27*, *28*), but the analysis has been encumbered by the extensive cloud cover associated with these storms. Figure 4 compares the TMI SST field with infrared SST imagery (*29*) of Hurricane Bonnie on 24 to 26 August 1998. The microwave imagery provides nearly complete coverage, whereas much of the infrared imagery is blocked by clouds. Figure 4 also illustrates another possible problem for the infrared retrievals. The Gulf Stream east of Cape Hatteras, which is clearly resolved in the microwave imagery, is barely visible in the infrared imagery. We attribute this to undetected clouds obscuring the ocean surface.

Storm track prediction has steadily improved along with better numerical models and observations, but the prediction of storm intensity falls short of expectations (*4*). Several studies (*4*, *30*) have shown that after initial development, the intensity of severe storms is strongly influenced by the thermodynamic structure of the upper ocean, and an accurate prediction of the storm's future intensity requires measurements of the ocean's thermal structure ahead of the storm. Extensive cloud cover around storms often prevents infrared satellite SST measurements. Microwave SST retrievals clearly have the potential to improve these important forecasts, as was shown in the 1998 hurricane season. In late August, Hurricane Danielle closely followed Hurricane Bonnie. Danielle's intensity dropped significantly as it passed over a region of cold water caused by Bonnie (Fig. 4A). Because of the cloud problem in infrared SST retrievals, the National Hurricane Center (NHC) uses a low-resolution SST field (measured weekly at a resolution of 100 km) (*8*) from the previous week (Fig. 4C) in their intensity models (*31*). For the Danielle prediction, this weekly SST product was missing Bonnie's cold wake, which may explain why most official forecasts overestimated Danielle's intensity by 30 to 40 knots (*32*).

TMI is the first in a series of satellite microwave radiometers that will measure SST under nearly all weather conditions. In the next 2 years, two Advanced Microwave Scanning Radiometers (AMSR) will be launched on U.S. and Japanese spacecraft. The AMSR will have an additional 6.9-GHz channel that will enhance SST retrieval. Later in the decade, the Conical Microwave Imager Sounder (CMIS) will be a primary sensor flying on the National Polar Orbiting Environmental Satellite System. CMIS, with its full complement of polarimetric channels, will be able to measure the global SST field to an accuracy of about 0.2°C at a spatial-temporal resolution of 50 km and 3 days.

References and Notes

1. M. A. Cane, S. E. Zebiak, S. C. Dolan, *Nature* **321**, 827 (1986).
2. M. J. McPhaden, *Science* **283**, 950 (1999).
3. M. DeMaria and J. Kaplan, *J. Clim.* **7**, 1324 (1994).
4. K. A. Emanuel, *Nature* **401**, 665 (1999).
5. D. Kamykowski, *Deep-Sea Res.* **34**, 1067 (1987).
6. E. P. McClain, W. G. Pichel, C. C. Walton, *J. Geophys. Res.* **90**, 11587 (1985).
7. R. Legeckis, *Science* **197**, 1177 (1977).
8. R. W. Reynolds and T. M. Smith, *J. Clim.* **7**, 929 (1994).
9. R. Legeckis, *J. Geophys. Res.* **91**, 12879 (1986).
10. F. M. Monaldo, T. D. Sikora, S. M. Babin, R. E. Sterner, *Mon. Weather Rev.* **125**, 2716 (1997).
11. R. W. Reynolds, C. K. Folland, D. E. Parker, *Nature* **341**, 728 (1989).
12. R. W. Reynolds, *J. Clim.* **6**, 768 (1993).
13. R. G. Lipes *et al.*, *Science* **204**, 1415 (1979).
14. R. Hofer, E. G. Njoku, J. W. Waters, *Science* **212**, 1385 (1981).
15. T. Liu, *J. Geophys. Res.* **93**, 6749 (1988).
16. C. Kummerow, W. Barnes, T. Kozu, J. Shiue, J. Simpson, *J. Atmos. Oceanic Technol.* **15**, 808 (1998).
17. The algorithm being used is an extension of the SSM/I ocean algorithm [F. J. Wentz, *J. Geophys. Res.* **102**, 8703 (1997)]. A set of four geophysical parameters (SST, wind speed, water vapor, and cloud water) is found that match the observations (from 10.7 to 37 GHz) to a simplified radiative transfer model.
18. M. J. McPhaden *et al.*, *J. Geophys. Res.* **103**, 14169 (1998).
19. D. B. Gilhousen, *J. Atmos. Oceanic Technol.* **4**, 94, (1987).
20. The difference between the ocean skin temperature and a bulk temperature has been studied in field experiments with infrared SST measurements made from ships [P. Schluessel, W. J. Emery, J. Grassl, T. Mammen, *J. Geophys. Res.* **95**, 13341 (1990)]. These field studies show maximum bulk skin temperature differences of ±1.0°C and mean offsets of 0.1°C for the day and 0.3°C for the night (skin cooler than bulk). The skin temperature measured by infrared sensors represents the upper few microns of the ocean rather than the 1-mm penetration depth of the microwaves. It is not clear how these infrared results translate to the microwave problem. For this study, no correction was made for the bulk-skin temperature difference, making it an additional source of error in the comparisons.
21. S. G. H. Philander, *J. Geophys. Res.* **83**, 3679 (1978).
22. D. B. Chelton, F. J. Wentz, C. L. Gentemann, R. A. de Szoeke, *Geophys. Res. Lett.*, in press.
23. J. M. Wallace, T. P. Michell, C. Deser, *J. Clim.* **2**, 1492 (1989).
24. S. P. Hayes, M. J. McPhaden, J. M. Wallace, *J. Clim.* **2**, 1500 (1989).
25. S. P. Xie, M. Ishiwatari, H. Hashizume, K. Takeuchi, *Geophys. Res. Let.* **25**, 3863 (1998).
26. W. T. Liu, K. B. Katsaros, J. A. Businger, *J. Atmos. Sci.* **36**, 1722 (1979).
27. P. G. Black and G. J. Holland, *Mon. Weather Rev.* **123**, 2007 (1995).
28. N. B. Nelson, *Mon. Weather Rev.* **126**, 1364 (1998).
29. J. Vazquez, K. Perry, K. Kilpatrick, *Tech. Rep. No. D-14070* (Jet Propulsion Laboratory, Pasadena, CA, 1996).
30. M. A. Saunders and A. R. Harris, *Geophys. Res. Lett.* **24**, 1255 (1997).
31. M. DeMaria and J. Kaplan, *Weather Forecasting* **9**, 209 (1994).
32. R. J. Pasch, *1998: Preliminary Report, Hurricane Danielle, 24 August–3 September 1998* (NHC, Miami, FL, 1999).

33. Supported by research contracts from NASA's Earth Science Program.

28 December 1999; accepted 10 March 2000

Cooperation Through Image Scoring in Humans

Claus Wedekind[1,2]*† and Manfred Milinski[1]‡

The "tragedy of the commons," that is, the selfish exploitation of resources in the public domain, is a reason for many of our everyday social conflicts. However, humans are often more helpful to others than evolutionary theory would predict, unless indirect reciprocity takes place and is based on image scoring (which reflects the way an individual is viewed by a group), as recently shown by game theorists. We tested this idea under conditions that control for confounding factors. Donations were more frequent to receivers who had been generous to others in earlier interactions. This shows that image scoring promotes cooperative behavior in situations where direct reciprocity is unlikely.

Cooperative behavior in social dilemma situations (*1*) can sometimes be understood as reciprocal altruism (*2*). However, humans often help others even if the altruistic act is not likely to be returned by the recipient (*3*). Recent computer simulations and analytical models (*4*–*6*) have shown that this can be beneficial in the long run and can be an evolutionarily stable strategy. The idea is that helping someone, or refusing to do so, has an